

Effect of inelastic scattering on underwater daylight in the ocean: model evaluation, validation, and first results

Marc Schroeder, Hans Barth, and Rainer Reuter

A model based on a matrix-operator theory capable of simulating underwater daylight in the ocean is presented. The main focus is on gelbstoff and chlorophyll fluorescence as well as water Raman scattering as sources of inelastic scattering and their effect on underwater daylight and relevance for the remote sensing of ocean color. Any combination of inelastic sources can be investigated, including differences in simulated underwater daylight in the absence and the presence of these sources. To our knowledge, it is the first matrix-operator model to include all these inelastic sources. The model allows simulations for case 1 and case 2 waters. Calculations can be done with highly anisotropic phase functions as they are observed in the ocean, and every order of multiple scattering is considered. A detailed mathematical description of inelastic sources is given, and a special treatment of the depth dependency of these sources is presented. The model is validated by comparison with depth-dependent and spectrally resolved measurements of downward irradiance in the open ocean. The differences between measured and simulated data are within the error of the radiometric measurements. Water Raman scattering has been found to contribute significantly to water-leaving radiance. The inelastic fraction depends on the water Raman scattering coefficient, on the ratio of the total attenuation coefficient at excitation and emission wavelengths, and on the spectral course of the irradiance incident on the ocean. For clear ocean waters the inelastic fraction can reach values of more than 17% [$C = 0.03 \text{ mg m}^{-3}$, $a_y(440 \text{ nm}) = 0.01 \text{ m}^{-1}$] at wavelengths relevant for the remote sensing of ocean color. The inelastic fraction of gelbstoff fluorescence can reach or even exceed the relevance of water Raman scattering at short wavelengths. In the water column, depending on optically active substances and on actual depth, water Raman scattering can provide 100% of the light field at wavelengths greater than 580 nm. The effect of gelbstoff fluorescence on depth-dependent irradiances is less significant than the effect of water Raman scattering in all cases considered, except for near surface levels and high gelbstoff concentrations.

© 2003 Optical Society of America

OCIS codes: 010.4450, 280.0280, 290.5860, 010.7340.

1. Introduction

Underwater daylight reveals some information on processes at the surface and within the ocean. The incident radiation is the main variable governing thermal heating and evaporation and is the energy source of photosynthesis. Photosynthesis binds CO_2 , a major greenhouse gas, and acts as a sink for

the gas owing to the sinking of organic detritus to depth. To model the CO_2 balance, knowledge of underwater daylight is necessary.

In past years the contribution of inelastic sources to underwater daylight, especially water Raman scattering and chlorophyll fluorescence, was found to be of great importance.¹⁻⁶ Raman scattered light provides at certain depths, besides sunlight-stimulated fluorescence at high concentrations of fluorophores, as much as 100% of the light field in the green- and red-wavelength range.

At the ocean surface the water-leaving radiance is affected by fluorescence and by water Raman scattering. The Raman fraction of the water-leaving radiance can exceed several percent of the total intensity at wavelengths relevant for ocean-color remote sensing.^{5,6} Several remote-sensing algorithms have been developed to derive information on water con-

M. Schroeder is with Freie Universität Berlin, Institut für Weltraumwissenschaften, Carl-Heinrich-Becker Weg 6-10, 12165 Berlin, Germany. H. Barth and R. Reuter are with Carl von Ossietzky Universität Oldenburg, Fachbereich Physik, Carl-von-Ossietzky Strasse, 26111 Oldenburg, Germany.

Received 27 August 2002; revised manuscript received 20 February 2003.

0003-6935/03/214244-17\$15.00/0

© 2003 Optical Society of America

stituents, either to describe their inherent optical properties⁷ or to estimate their concentrations.^{8–12} One needs to adjust ocean-color algorithms for fluorescence and water Raman scattering as well as for the high concentrations and variabilities of water constituents in coastal regions,^{10,12–14} to evaluate satellite measurements of water-body reflectivities.

Various water constituents causing different processes such as absorption, scattering, and fluorescence alter the underwater daylight in a wavelength-, depth-, and angular-dependent way. An overview of optically relevant water constituents is given by Mobley.¹⁴ All optical processes affecting underwater daylight are mathematically described by the radiative-transfer equation (RTE). Several approaches have been used to solve the RTE: discrete ordinates (e.g., Jin and Stamnes¹⁵), Monte Carlo methods (e.g., Stavn and Weidemann¹⁶), or the matrix-operator theory (e.g., Plass *et al.*¹⁷ and Fell and Fischer¹⁸). In this paper an algorithm based on the matrix-operator theory is used because of the great physical insight of the fundamental equations of the matrix-operator theory and the short computing times for homogeneous layers. Following a short introduction into the matrix-operator theory, the incorporation of inelastic sources is presented. The model is validated by comparing simulated data with measurements of spectrally and depth-resolved irradiances in the open ocean.

2. Matrix-Operator Theory

The matrix-operator theory is a rigorous and illustrative method for solving the RTE for a layered medium, especially media of high optical thickness and highly anisotropic phase function. The theory is based on reflection and transmission processes that are introduced under reference to the interaction principle. On the basis of the research of Ambarzumian,¹⁹ Stokes,²⁰ and Chandrasekhar,²¹ Redheffer²² constructed an algebra for the reflection and the transmission operators, relating the operators of a combined layer to those of its own and including a procedure to derive the operators of very thin so-called elementary layers. Preisendorfer²³ applied the formalism to radiative transfer. Internal sources were added by Grant and Hunt.²⁴ A detailed overview was given by Plass *et al.*,¹⁷ which, together with the research of Fell and Fischer,¹⁸ is the basis of our model.

It is advantageous to introduce notations for brevity. The diffuse radiance L is a function of the cosine of the nadir angle μ and the azimuth angle ϕ : $L(\xi) = L(\mu; \phi)$. The set of all directions ξ gives the sphere Ξ , which can be divided in an upward and a downward hemisphere of directions (Ξ_u and Ξ_d , respectively). L^+ and L^- are the downward and the upward radiances, respectively, while L' denotes incident radiances. After the azimuth and the nadir angle are separated, L becomes a column matrix for a discrete set of μ .

The layer boundaries are indicated starting from the top of the medium by the optical thickness τ_0 ,

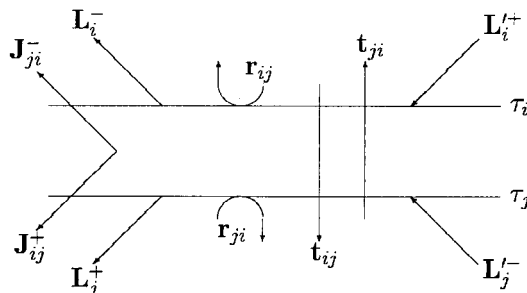


Fig. 1. Introduction of matrix operators.

τ_1, \dots, τ_K (where K is the number of homogeneous layers). The radiance at each layer boundary is denoted by $L(\tau_k) = L_k$ ($k = 0, 1, \dots, K$).

Integrating the radiance L over all solid angles of the sphere Ξ gives the total scalar irradiance E_0 , while the downward (plane) irradiance E_d and upward (plane) irradiance E_u are defined as the integral of $L(\mu)|\mu|$ over all solid angles of the hemispheres Ξ_d and Ξ_u , respectively. The vector irradiance is determined by the difference between E_d and E_u .

A. Basic Principles and Methods

The starting point of the matrix-operator theory is the interaction principle. It describes the interaction of light and matter as a linear process and on a phenomenological level. The linear relationship is based on reflection and transmission processes, while the latter means that macroscopic variables are introduced on the basis of observations and geometric optics.^{14,18} It follows from the interaction principle that the radiance leaving any considered layer depends linearly on incident radiances L'^{\pm} and sources J within the layer. With the definition of the transmission operator t_{01} and the radiance L expressed as a vector,

$$\int t_{01}(\mu' \rightarrow \mu) L_0'^+(\mu') d\mu' = t_{01} L_0'^+ \quad (1)$$

($\mu \in [0, 1]$) and the correspondingly defined matrix operators t_{10} , r_{10} , and r_{01} , the interaction principle leads to the basic equations for calculating the underwater daylight at internal layer boundaries and, after some simplifications, the medium leaving radiances:

$$L_i^+ = (\mathbf{E} - \mathbf{r}_{i0} \mathbf{r}_{ij})^{-1} (\mathbf{r}_{i0} \mathbf{t}_{ji} L_j'^- + \mathbf{t}_{0i} L_0'^+ + \mathbf{r}_{i0} \mathbf{J}_{ji}^- + \mathbf{J}_{0i}^+), \quad (2)$$

$$L_i^- = (\mathbf{E} - \mathbf{r}_{ij} \mathbf{r}_{i0})^{-1} (\mathbf{r}_{ij} \mathbf{t}_{0i} L_0'^+ + \mathbf{t}_{ji} L_j'^- + \mathbf{r}_{ij} \mathbf{J}_{0i}^+ + \mathbf{J}_{ji}^-), \quad (3)$$

with $j = i + 1$ ($i \in [1, K]$) and the identity matrix \mathbf{E} . K is the number of internal layers. In Subsection 2.B the column matrix operators L and J are discussed and are normally not treated as vector operators.^{17,18} Figure 1 shows an overview of the matrix operators.

The sea surface and the sea floor are treated as

independent layers with indices $k = 0, k = 1$ (τ_{01}) and $k = K, k = K + 1$ ($\tau_{K, K+1}$), respectively.

Matrix operators \mathbf{r}_{i0} , \mathbf{t}_{0i} , and \mathbf{J}_{0i}^+ are determined by the so-called adding procedure. The adding procedure gradually combines the operators of each homogeneous layer:

$$\mathbf{r}_{j0} = \mathbf{r}_{ji} + \mathbf{t}_{ij}(\mathbf{E} - \mathbf{r}_{i0}\mathbf{r}_{ij})^{-1}\mathbf{r}_{i0}\mathbf{t}_{ji}, \quad (4)$$

$$\mathbf{t}_{0j} = \mathbf{t}_{ij}(\mathbf{E} - \mathbf{r}_{i0}\mathbf{r}_{ij})^{-1}\mathbf{t}_{0i}, \quad (5)$$

$$\mathbf{J}_{0j}^+ = \mathbf{J}_{ij}^+ + \mathbf{t}_{ij}(\mathbf{E} - \mathbf{r}_{i0}\mathbf{r}_{ij})^{-1}(\mathbf{r}_{i0}\mathbf{J}_{ji}^- + \mathbf{J}_{0i}^+). \quad (6)$$

The remaining operators of Eqs. (2) and (3), \mathbf{r}_{ij} , \mathbf{t}_{ji} , and \mathbf{J}_{ji}^- , are determined by the so-called doubling procedure. To avoid confusion between adding and doubling indices, two adjacent layers with exemplary indices 0 and 1 as well as 1 and 2 (layers τ_{01} and τ_{12} , respectively) are considered to introduce the doubling procedure. Doubling can be carried out if the layer is homogeneous (e.g., $\mathbf{t}_{01} = \mathbf{t}_{12} = \mathbf{t}_1$) and the phase function is symmetric (e.g., $\mathbf{r}_{12} = \mathbf{r}_{21} = \mathbf{r}_1$). We have

$$\mathbf{r}_{02} = \mathbf{r}_{20} = \mathbf{r}_2 = \mathbf{r}_1 + \mathbf{t}_1(\mathbf{E} - \mathbf{r}_1\mathbf{r}_1)^{-1}\mathbf{r}_1\mathbf{t}_1, \quad (7)$$

$$\mathbf{t}_{02} = \mathbf{t}_{20} = \mathbf{t}_2 = \mathbf{t}_1(\mathbf{E} - \mathbf{r}_1\mathbf{r}_1)^{-1}\mathbf{t}_1, \quad (8)$$

$$\mathbf{J}_{02}^+ = \mathbf{J}_{12}^+ + \mathbf{t}_1(\mathbf{E} - \mathbf{r}_1\mathbf{r}_1)^{-1}(\mathbf{r}_1\mathbf{J}_{21}^- + \mathbf{J}_{01}^+), \quad (9)$$

$$\mathbf{J}_{20}^- = \mathbf{J}_{10}^- + \mathbf{t}_1(\mathbf{E} - \mathbf{r}_1\mathbf{r}_1)^{-1}(\mathbf{r}_1\mathbf{J}_{01}^+ + \mathbf{J}_{21}^-). \quad (10)$$

We denote layers required for the doubling procedure as numerical layers. Matrix operators \mathbf{r}_{01} , \mathbf{r}_{10} , \mathbf{t}_{01} , and \mathbf{t}_{10} can be determined only for a so-called elementary layer with a thickness of less than $\Delta\tau \leq 2^{-15}$.¹⁷ The matrix-operator theory is fast for computing underwater daylight for a homogeneous water body because of the doubling of the layer thickness in each step of the doubling procedure. The doubling procedure cannot be applied to source operators because of their depth dependency. This issue is discussed in Section 4.

Simulation of underwater daylight requires the following steps: First, an approximation of the depth dependency of optically relevant properties of a considered water body is required. Then we can apply the doubling procedure [Eqs. (7)–(10)] to determine the reflection, transmission, and source operators of each homogeneous layer. The adding procedure [Eqs. (4)–(6)] gradually combines the results of the doubling procedure to receive the operators of the whole water body. Starting at the seafloor, and with the help of Eqs. (2) and (3), we can determine the underwater daylight.

B. Radiative-Transfer Equation and Matrix Operators

The aim of this section is to give a brief overview of the derivation of the matrix operators \mathbf{r} and \mathbf{t} for an elementary layer and to point out a few special items of this work that differ from the usual treatment in matrix-operator theory.

The starting point is the RTE that governs the behavior of light within natural water bodies. If polarization effects, the conversion of nonradiometric

energies, and changes in the refractive index are neglected, the stationary RTE for a horizontally homogeneous medium is

$$\begin{aligned} \mu \frac{dL(\tau; \xi; \lambda)}{d\tau} = & -L(\tau; \xi; \lambda) \\ & + \omega_0 \int_{\Xi} \tilde{\beta}(\tau; \xi' \rightarrow \xi; \lambda) \\ & \times L(\tau; \xi'; \lambda) d\Omega(\xi') \\ & + \omega_0 \tilde{\beta}(\tau; \xi_0 \rightarrow \xi; \lambda) F_0 \exp(-\tau/\mu_0) \\ & + \frac{1}{c} L_*^I(\tau; \xi; \lambda), \end{aligned} \quad (11)$$

where L is composed of the direct and the diffuse spectral radiance, L_*^I combines all inelastic scattering processes, c is the total beam attenuation coefficient, ω_0 is the single-scattering albedo, F_0 is the direct irradiance just below sea surface level, and ξ_0 is the direction of the direct sunlight, defined by the cosine of the solar zenith angle μ_0 and the solar azimuth angle ϕ_0 . The phase function $\tilde{\beta}$ is considered in detail in Appendix A.

After we focus on the diffuse spectral radiance, a first step in the procedure for deriving the matrix operators is the separation of the azimuth and nadir dependency, which results in a considerable decrease in computation time.¹⁸ For the purpose of separation the phase function $\tilde{\beta}$ and the diffuse radiance L are expressed in a Fourier series. Here only azimuthally averaged phase functions and radiances are considered. Owing to azimuth averaging and the assumption of horizontal homogeneity, the incident azimuth angle is set to zero.

The main goal of this paper is the estimation of the influence of fluorescence and water Raman scattering on underwater daylight. To determine the source terms, irradiances are needed that can be exactly calculated by using azimuthally averaged radiances (Ref. 1 and Subsections 3.A and 3.B.).

The next steps are the differentiation of downward and upward radiances and the discretization of the nadir angle μ to determine the integrals of the spatially redistributed incoming radiances:

$$\int_0^1 f(\mu) d\mu = \sum_{i=1}^N f(\mu_i) c_i + R(N). \quad (12)$$

$R(N)$ is the remaining error and N is the number of discretization points (see Ref. 25 for details). In this paper the Gauss–Lobatto quadrature scheme is used. The RTE can then be expressed in matrix form.¹⁷

Redheffer²² and Grant and Hunt²⁴ derived an equation system for downward and upward radiances, allowing determination of matrix operators \mathbf{r}

and \mathbf{t} by applying and comparing their equations to the RTE in matrix form:

$$(\mathbf{t}_{10} = \mathbf{t}_{01} =) \mathbf{t} = \mathbf{E} - \Delta\tau \mathbf{M}^{-1}(\mathbf{E} - \omega_0 2\pi \tilde{\beta}^{++} \mathbf{C}), \quad (13)$$

$$(\mathbf{r}_{10} = \mathbf{r}_{01} =) \mathbf{r} = \Delta\tau \omega_0 2\pi \mathbf{M}^{-1} \tilde{\beta}^{-+} \mathbf{C}, \quad (14)$$

where $\mathbf{M} = [\mu_j \delta_{jk}]$, $\mathbf{C} = [c_j \delta_{jk}]$, $\tilde{\beta}^{++} = [\tilde{\beta}(\mu_{j'} \rightarrow \mu_i)]$, $\tilde{\beta}^{-+} = [\tilde{\beta}(-\mu_{j'} \rightarrow \mu_i)]$, and \mathbf{E} is the identity matrix.

With the help of Eqs. (13) and (14) the matrix operators for an elementary layer can be determined. Equation (14) can be applied only if no multiple scattering occurs. According to Plass *et al.*¹⁷ Eq. (14) is valid for $\Delta\tau \leq 2^{-15}$.

We define two single-column matrices $\tilde{\beta}_0^+ = [\tilde{\beta}(\mu_0 \rightarrow \mu_i)]$ and $\tilde{\beta}_0^- = [\tilde{\beta}(\mu_0 \rightarrow -\mu_i)]$ as the phase-function vectors for the solar zenith angle. Despite the usual treatments,^{17,18} they are independent matrix operators. The computing time decreases since the source operators for the scattered direct sunlight as well as the inelastic source operators and the radiances can be expressed as single-column matrices. If the solar zenith angle μ_0 is not part of the set of abscissas μ_i , it will be added and the corresponding weight c_i will be set to zero.

Incorporation of elastic source terms caused by scattering of direct sunlight \mathcal{J}^S and its reflection at the sea floor is discussed by Fell and Fischer.¹⁸

3. Inelastic Sources

Inelastic source terms incorporated in the model are gelbstoff and chlorophyll fluorescence (\mathcal{J}^Y , \mathcal{J}^C , respectively) and water Raman scattering \mathcal{J}^R , all resulting in a wavelength shift in the absorbed and the reemitted radiation.^{13,14} To determine the excitation energy, a first model run is necessary. When the excitation energy is known and with the help of the expressions in this section, a second model run leads to the final result.

The algorithm enables the user to choose between any combination of \mathcal{J}^Y , \mathcal{J}^C , and \mathcal{J}^R . In particular, the difference in the simulated radiances in the absence and presence of inelastic scattering can be investigated.

A. Gelbstoff and Chlorophyll Fluorescence

In this section we deal with the inelastic source terms of gelbstoff and chlorophyll fluorescence, and we orient it at the work of Gordon,²⁶ Traganza,²⁷ Haltrin and Kattawar,² Kirk,¹³ and Mobley.¹⁴ Chlorophyll is required for any photosynthetic process in plants, in particular in phytoplankton.¹³ Gelbstoff, or yellow substance, is the uncharacterized light-absorbing fraction of dissolved organic carbon, formed from the degradation products of animals and plants.

Formally, fluorescence can be described as absorption and elastic scattering. Light from the whole range of relevant excitation wavelengths $\Lambda^{C,Y}$ contributes to the radiance at a given emission wavelength. Contributions from all incident directions to a certain scattering angle must be integrated over all

solid angles Ω if the spatial dependency of the inelastically scattered light is considered:

$$\begin{aligned} J^{C,Y}(\xi; \lambda) &= \frac{1}{c(\lambda)} \int_{\Lambda^{C,Y}} \int_{\Xi} \beta^{C,Y}(\xi' \rightarrow \xi; \lambda) \\ &\quad \times L(\xi'; \lambda') d\Omega(\xi') d\lambda', \end{aligned} \quad (15)$$

where $\beta^{C,Y} = b^{C,Y} \tilde{\beta}^{C,Y}$ is the volume scattering function, where $b^{C,Y}$ is the scattering coefficient for gelbstoff or chlorophyll fluorescence; $b^{C,Y}$ describes the reemission of the absorbed light according to a redistribution function $f^{C,Y}$:

$$b^{C,Y}(\lambda' \rightarrow \lambda) = a_{C,Y}(\lambda') f^{C,Y}(\lambda' \rightarrow \lambda), \quad (16)$$

where a_C and a_Y are the absorption coefficients of chlorophyll and gelbstoff, respectively. If $f^{C,Y}$ is expressed in terms of the quantum efficiency function $\eta^{C,Y} = \eta^{C,Y}(\lambda' \rightarrow \lambda)$, defined as the number of photons emitted at λ per unit wavelength interval normalized on the number of photons absorbed at λ' , it follows after converting photon counts to energy that $f^{C,Y} = \eta^{C,Y} \lambda' / \lambda$. The $\eta^{C,Y}$ can be interpreted as the product of the quantum efficiency $\Phi^{C,Y}$ (number of photons emitted at λ normalized on the number of photons absorbed at λ') and the normalized emission function $h^{C,Y}$; $h^{C,Y}$ gives the spectral dependency of the emitted light and has units of nm^{-1} . If a nondimensional function $g^{C,Y}$ is introduced that specifies the interval over which light is able to excite fluorescence, then $g^{C,Y} \Phi^{C,Y}$ is a measure for that part of the absorbed light that will be reemitted. Summarizing, Eq. (16) becomes

$$b^{C,Y}(\lambda' \rightarrow \lambda) = a_{C,Y}(\lambda') \Phi^{C,Y}(\lambda') g^{C,Y}(\lambda') h^{C,Y}(\lambda) \frac{\lambda'}{\lambda}, \quad (17)$$

where g^C is 1 in the interval $370 \leq \lambda' \leq 690$ nm and 0 elsewhere and g^Y is 1 in the interval $250 \leq \lambda' \leq 400$ nm and 0 elsewhere; $h^{C,Y}$ is approximated by a Gauss function.^{26,27,2}

A possible wavelength dependency of quantum efficiencies Φ^C and Φ^Y is neglected. Using the work of Hawes *et al.*,²⁸ Kiefer and Reynolds,²⁹ and Kiefer *et al.*³⁰ and references therein, Mobley¹⁴ gave the following efficiencies: $\Phi^C \in [0.01, 0.1]$ with values between 0.01 and 0.05 being typical and $\Phi^Y \in [0.005, 0.015]$. Kirk¹³ confirmed the lower value of $\Phi^C = 0.01$, with an increase to ~ 0.03 if photosynthesis is inhibited. Günther *et al.*⁸ gave a range from $\Phi^C = 0.0015$ to 0.1 with a typical value of 0.0035. Comparing measurements in the North Sea and radiative-transfer simulations, Fischer *et al.*³¹ and Doerffer and Fischer³² found a value of $\Phi^C = 0.003$. An approximation of the wavelength dependency of gelbstoff fluorescence can be found in Hawes *et al.*,²⁸ Green and Blough,³³ and Coble.³⁴

It is common to assume an isotropic phase function $\tilde{\beta}^{C,Y}(\xi' \rightarrow \xi) = 1/(4\pi)$ (in units of sr^{-1}),¹⁴ and therefore it is not necessary to carry out a separation of the azimuth and nadir angle dependency.

Taking all this into account, Eq. (15) becomes

$$\begin{aligned} J^{C,Y}(\lambda) &= \frac{\Phi^{C,Y} h^{C,Y}(\lambda)}{4\pi c(\lambda)\lambda} \int_{\lambda_{C,Y}} a_{C,Y}(\lambda') g^{C,Y}(\lambda') E_0(\lambda') \lambda' d\lambda' \\ &= \frac{\Phi^{C,Y} h^{C,Y}(\lambda)}{4\pi c(\lambda)\lambda} A^{C,Y}(\lambda). \end{aligned} \quad (18)$$

The last step in incorporating J^Y and J^C into the matrix-operator theory is the application of the discretization and the expression in matrix form. $A^{C,Y}$ [Eq. (18)] is expressed as a single-column matrix with N elements [Eq. (12)]. If the fluorescence source term is determined for an optical thin layer ($\Delta\tau \ll 1$) and the results of Subsection 2.B. are used, one gets

$$\mathbf{J}^{C,Y}(\Delta\tau; \tau; \lambda) = \Delta\tau \frac{\Phi^{C,Y} h^{C,Y}(\lambda)}{4\pi c(\lambda; \tau)\lambda} \mathbf{M}^{-1} \mathbf{A}^{C,Y}(\lambda; \tau). \quad (19)$$

A maximum wavelength increment of 10 nm was suggested by Fell and Fischer.¹⁸

B. Water Raman Scattering

Raman scattering is produced by water itself and therefore occurs in all water bodies. The dominant Raman line results from the O–H stretch mode. Raman scattering depends on temperature and salinity,^{35,36} which is neglected here.

The procedure of the incorporation of water Raman scattering into the matrix-operator theory is similar to the procedure for fluorescence (Subsection 3.A). The reemission of light is described by the water Raman scattering coefficient b^R :

$$b^R(\lambda' \rightarrow \lambda) = a^R(\lambda') f^R(\lambda' \rightarrow \lambda), \quad (20)$$

where f^R is the redistribution function of water Raman scattering and a^R is the water Raman absorption coefficient:

$$a^R(\lambda') = a_0^R(\lambda_0') \left(\frac{\lambda_0'}{\lambda'} \right)^n. \quad (21)$$

In the literature different values of $a_0^R(\lambda_0')$ and n can be found.^{1,3,37} The values of $a_0^R(\lambda_0')$ differ by a factor of 5. Marshall and Smith³ summarized the measurements and confirmed the lower values. Bartlett *et al.*³⁷ retrieved almost exactly the same result for $a_0^R(\lambda_0')$ as Marshall and Smith³ but additionally closely investigated the wavelength dependency of a^R . Their quantities for excitation wavelengths and for units of energy are used here: $a_0^R = (2.7 \pm 0.2) \times 10^{-4} \text{ m}^{-1}$ at $\lambda_0' = 488 \text{ nm}$ and $n = 5.5$.

The f^R can be expressed by a sum of four Gauss functions as Walrafen did.^{35,38} If that result is ex-

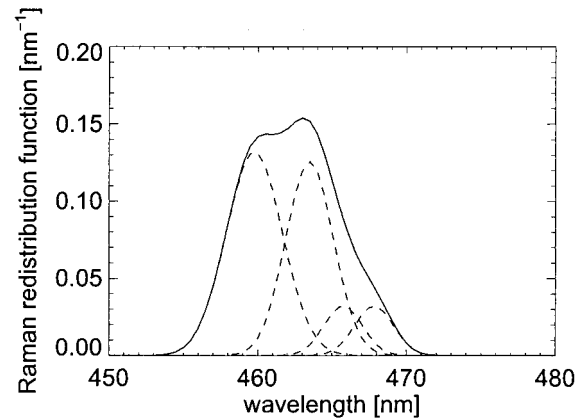


Fig. 2. Composition of, solid curve, the redistribution function of water Raman scattering of, dashed curves, four Gauss functions for an exemplary excitation wavelength of 400 nm.

pressed in wavelengths λ instead of wave numbers $\tilde{\nu}$, we get

$$\begin{aligned} f^R(\lambda' \rightarrow \lambda) &= \frac{10^7}{\lambda'^2} \frac{1}{(2\pi)^{1/2} \sum_{i=1}^4 (\alpha_i \sigma_i)} \sum_{i=1}^4 \alpha_i \\ &\times \exp \left[- \frac{\left(\frac{10^7}{\lambda'} - \frac{10^7}{\lambda} - \Delta\tilde{\nu}_i \right)^2}{2\sigma_i^2} \right]. \end{aligned} \quad (22)$$

Equation (22) is valid for $\lambda' \leq \lambda$ and zero otherwise (λ in nanometers). The coefficients are taken from Haltrin and Kattawar.²

Figure 2 demonstrates the composition of the redistribution function of Raman scattering (solid curve) of four Gauss functions (dashed curves) and its spectral dependency for an excitation wavelength of 400 nm. Figure 3 illustrates the dependency of f^R on different excitation wavelengths: With increasing excitation wavelength, f^R broadens and its maximum decreases.

The water Raman volume scattering function β^R is

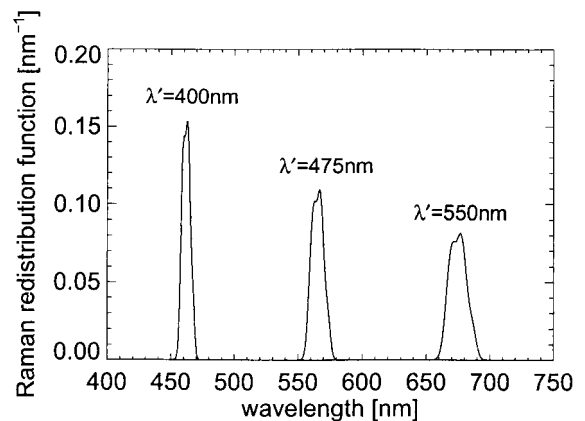


Fig. 3. Raman redistribution function for three different excitation wavelengths.

not isotropic as with gelbstoff and chlorophyll fluorescence. Porto³⁹ expressed β^R as follows:

$$\beta^R(\psi; \lambda' \rightarrow \lambda) = \frac{3}{16\pi} \left(\frac{1+3\rho}{1+2\rho} \right) \times [1 + \gamma \cos^2(\psi)] b^R(\lambda' \rightarrow \lambda), \quad (23)$$

where ψ is the scattering angle, ρ is the depolarization ratio, and $\gamma = (1-\rho)/(1+3\rho)$. The dependency of ρ on the Raman shift $\lambda' \rightarrow \lambda$ is neglected here.¹ Instead a value of $\rho = 0.17$ is used. To incorporate Raman scattering into the matrix-operator theory, Eq. (23) is rewritten with the help of Legendre polynomials:

$$\beta^R(\psi; \lambda' \rightarrow \lambda) = \frac{3}{16\pi} \left(\frac{1+3\rho}{1+2\rho} \right) \left[1 + \frac{1}{3} \gamma + \frac{2}{3} \gamma P_2(\cos \psi) \right] b^R(\lambda' \rightarrow \lambda), \quad (24)$$

with $P_2 = \frac{1}{2}[3 \cos^2(\psi) - 1]$. If Eq. (24) is compared with a general Legendre polynomial²¹ for β^R ,

$$\beta^R(\psi; \lambda' \rightarrow \lambda) = \frac{1}{4\pi} \sum_{l=0}^N b_l^R(\lambda' \rightarrow \lambda) P_l(\cos \psi), \quad (25)$$

one finds

$$b_0^R(\lambda' \rightarrow \lambda) = b^R(\lambda' \rightarrow \lambda), \quad (26)$$

$$b_2^R(\lambda' \rightarrow \lambda) = \frac{1}{2} \left(\frac{1-\rho}{1+2\rho} \right) b^R(\lambda' \rightarrow \lambda). \quad (27)$$

With the azimuthally averaged radiance L , when $P_l(\cos \psi)$ is rewritten with consideration of the addition theorem of Legendre polynomials,²¹ and Eqs. (26) and (27) are used, Eq. (15) becomes (indices C, Y replaced by R)

$$\begin{aligned} \mathcal{J}^R(\mu; \lambda) &= \frac{1}{4\pi c(\lambda)} \int_{\Lambda^R} b^R(\lambda' \rightarrow \lambda) \left\{ E_0(\lambda') \right. \\ &\quad \left. + \frac{1}{2} \left[\frac{1-\rho}{1+2\rho} E_2(\mu; \lambda') P_2(\mu) \right] \right\} d\lambda' \\ &= \frac{1}{4\pi c(\lambda)} A^R(\mu; \lambda). \end{aligned} \quad (28)$$

The first part of the integral would be the result for an isotropic case, while the second part corrects the source term due to the nonisotropic Raman volume scattering function. We get, similar to Eq. (19), expressed in matrices:

$$\mathbf{J}^R(\Delta\tau; \tau; \mu; \lambda) = \Delta\tau \frac{1}{4\pi c(\lambda; \tau)} \mathbf{M}^{-1} \mathbf{A}^R(\lambda; \mu; \tau). \quad (29)$$

In matrix-operator theory the excitation wavelengths are identical with those of the reemitted light. The redistribution function $f^R(\lambda' \rightarrow \lambda)$ [Eq. (22)] governs the relationship between absorption

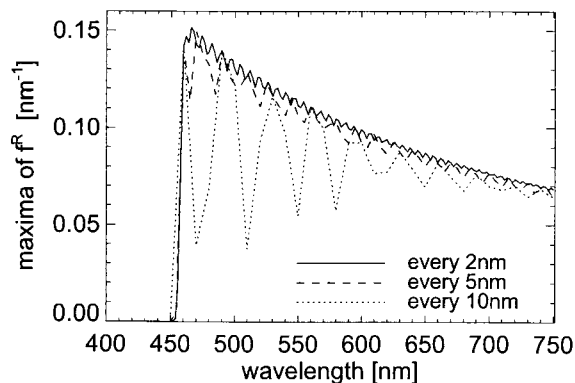


Fig. 4. Maxima of the redistribution function f^R of water Raman scattering for three different wavelength increments.

and reemission at higher wavelengths. Figure 3 demonstrates the relatively narrow shape of f^R for some exemplary excitation wavelengths at highly resolved emission wavelengths. If the redistribution function shown in Fig. 3 had been calculated with a high increment of a high emission wavelength, e.g., 10 nm, the shape of f^R for each excitation wavelength would have been completely different. The maximum values especially would be smaller than in Fig. 3. The consequence would be a strong underestimation of the reemitted light. For three different wavelength increments, the maxima of f^R depending on discrete emission wavelengths are shown in Fig. 4. For increments of $\Delta\lambda \leq 2$ nm the fluctuations are less than 5% if $\lambda' \geq 400$ nm.

4. Depth Dependency of the Source Operators

Owing to their depth dependency, we cannot apply the doubling procedure (Subsection 2.A) to the source operators $\mathcal{J}^{S,R,C,Y}$. \mathcal{J}^S is incorporated as discussed in Fell and Fischer¹⁸ by assuming an exponential decay of \mathcal{J}^S . This assumption does not hold for inelastic source operators owing to the dependence of the excitation energies on the optical depth and multiple scattering. The modified doubling procedure for inelastic source operators is a new development and avoids any approximations concerning depth dependency.

The excitation energy for fluorescence and water Raman scattering is determined at the boundary of every numerical layer. The inelastic source operators for an elementary layer at each numerical layer boundary can be calculated by Eqs. (19) and (29). A matrix \mathbf{f}_2 is defined to relate the source operator of the elementary layer and the corresponding numerical layer:

$$\mathbf{J}_{02}^+(\mu_i; \lambda) = \mathbf{f}_2(\mu_i; \lambda) \mathbf{J}_{01}^+(\mu_i; \lambda). \quad (30)$$

In Eqs. (30)–(33) the multiplications have to be carried out element-wise. The optical depth indices of \mathbf{J} are numbered as 0, 1, 2, 4, 8, . . . , whereas an index difference of 1 indicates an operator of an elementary

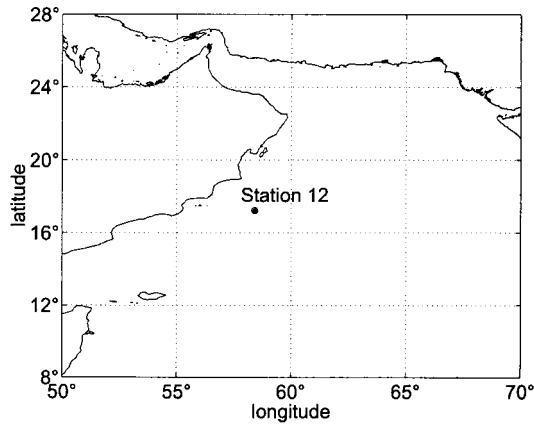


Fig. 5. Location of station 12.

layer. The \mathbf{f}_2 is used to determine the source term of the adjacent lower numerical layer:

$$\mathbf{J}_{24}^+(\mu_i; \lambda) = \mathbf{f}_2(\mu_i; \lambda) \mathbf{J}_{23}^+(\mu_i; \lambda). \quad (31)$$

With Eq. (9) we get \mathbf{J}_{04}^+ and define a new multiplier \mathbf{f}_4 :

$$\mathbf{J}_{04}^+(\mu_i; \lambda) = \mathbf{f}_4(\mu_i; \lambda) \mathbf{J}_{01}^+(\mu_i; \lambda), \quad (32)$$

from which we get, in the same manner as for Eq. (31),

$$\mathbf{J}_{48}^+(\mu_i; \lambda) = \mathbf{f}_4(\mu_i; \lambda) \mathbf{J}_{45}^+(\mu_i; \lambda). \quad (33)$$

If we proceed for each numerical layer, we are able to determine \mathbf{J}^+ for the whole homogeneous layer. \mathbf{J}^- is determined in exactly the same way as outlined above.

The modified doubling procedure is exact if the ratios of the inelastic sources at the elementary layers to the inelastic sources of the corresponding numerical layer are identical. Because of the homogeneity of each numerical layer, this seems reasonable.

5. Validation

A. General Approach

To investigate the accuracy and applicability of the model, we compared its results with spectral and depth-dependent downward irradiance measurements performed with a multispectral photometer (radiometer) in the open ocean. The comparison was carried out at four wavelengths (429, 489, 555, 641 nm) and over a depth range of 0–45 m.

The measurements used for the validation were carried out during a Joint Global Ocean Flux Study (JGOFS) campaign in the Indian Ocean in May 1997.⁴⁰ We have chosen the data received at station 12 (see Fig. 5) where an almost homogeneous water body in the upper 45 m had been observed. Figure 6 shows the temperature and salinity profiles and Fig. 7 the chlorophyll and gelbstoff fluorescence profiles measured at this station, both proving the homogeneity.

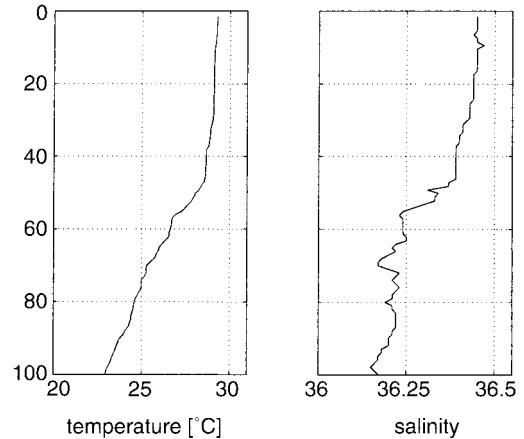


Fig. 6. Measured temperature and salinity at station 12.

Several parameters necessary for determining underwater daylight were measured during the campaign but unfortunately not a complete parameter set required as input for a simulation. Using the measured values and making appropriate assumptions for the unknown parameters, we did a first simulation. By comparing the radiometer measurements with the model output, we slightly adjusted the parameters.

B. Radiometer

A multispectral photometer developed to measure irradiances in the ocean was utilized during the JGOFS campaign,⁴¹ equipped with a cosine collector to determine the upward and downward irradiances E_u and E_d , respectively.

The light transmitted through each collector reaches two Carl Zeiss monolithic miniature spectrometer modules via an optical fiber. The monolithic miniature spectrometer prototypes used on this JGOFS cruise had the following set of wavelengths: $\lambda_i = 336.08 \text{ nm} + i6.638 \text{ nm}$ with $i = 1, \dots, 66$. Owing to data-transfer restrictions, only 82 selectable diodes transfer data to the board unit. Additionally, the integration time, which adjusts au-

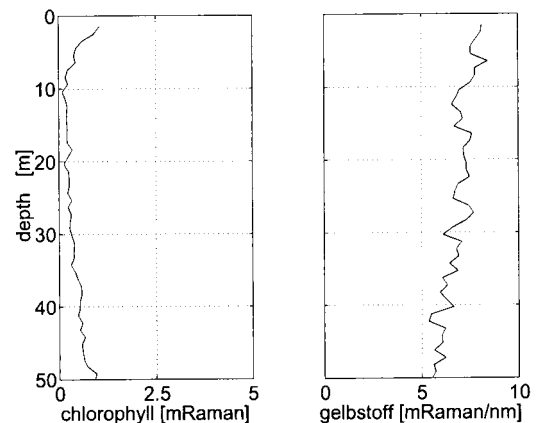


Fig. 7. Measured gelbstoff and chlorophyll fluorescence at station 12.

Table 1. Set of User Defined Parameters Taken as a Model Input

Parameter	Designation	Value
θ_0	Zenith angle of the Sun	10.6°
N_A	Atmospheric abscissas	15
N_O	Oceanic abscissas	17
H_{Ozon}	Reduced ozone height	0.2 cm
vis	Visibility	5 km, Summer model
λ	Wavelength	Every 2 nm from 250 to 650 nm plus 429, 489, 555, and 641 nm
ϵ	Accuracy	0.05%
z_B	Depth of the ocean ground	100 m
A_p	Ocean-ground reflectivity	0.0
C	Phytoplankton concentration	0.085 mg m ⁻³
Φ^C	Quantum efficiency of chlorophyll fluorescence	0.04
Φ^X	Quantum efficiency of gelbstoff fluorescence	0.01
$b_p(400\text{ nm})$	Particle scattering coefficient at 400 nm	0.036 m ⁻¹
c_j	Junge coefficient	4.1
$a_y(440\text{ nm})$	Absorption of gelbstoff at 440 nm	0.014 m ⁻¹
s	Slope parameter of gelbstoff absorption	0.017 nm ⁻¹

tomatically to the light intensity to improve the dynamic range, and the dark currents for both collectors are transmitted to the board unit.

The measured signals are processed with respect to integration time, dark currents, and the immersion effect before the absolute calibration is done. An error of 5.8% (6.4%) has been determined for the absolute calibration of the downward (upward) irradiance collector.

C. Parameters

The scattering properties of seawater are described by the theory of Einstein and Smoluchowsky.¹⁴ The water-absorption coefficients are taken from Pope and Fry⁴² for wavelengths between 380 and 727.5 nm and from Smith and Baker⁴³ for wavelengths between 250 and 380 nm.

The absorption of phytoplankton and nonchlorophyllous particles, either of biogenic or terrestrial origin, was determined by following Prieur and Sathyendranath⁴⁴ for wavelengths between 400 and 700 nm. Between 250 and 400 nm the absorbance measurements of Babin and Stramski⁴⁵ were used. They investigated four phytoplankton species, two of which do not exhibit an absorption maximum in the UV. The absorbance data of these two species are averaged after normalization and scaled based on their value and the value of Prieur and Sathyendranath⁴⁴ at 400 nm. The spectral scattering coefficient of particles b_p is calculated with the assumption of a Junge (hyperbolic) particle-size distribution (c_j , Junge coefficient):

$$b_p(\lambda) = b_p(400\text{ nm}) \left(\frac{\lambda}{400\text{ nm}} \right)^{3-c_j} \quad (34)$$

Petzold's measured phase functions and their parameterization with the particle-scattering coefficient are utilized (Appendix A).

The spectral characteristics of the gelbstoff absorp-

tion coefficient a_y in the near-surface layer follows an exponential law⁴⁶:

$$a_y(\lambda) = a_y(440\text{ nm}) \exp[-s(\lambda - 440\text{ nm})] \quad (35)$$

The slope parameter s has a value of 0.014 nm⁻¹ typically. Except for a slight discontinuity around 325 or 350 nm,⁴⁶ Eq. (35) is in good agreement with the measurements.^{46,47}

The atmospheric part of the model needs two optically relevant parameters as user-defined input. The reduced ozone height H_{Ozon} is necessary to determine the optical depth based on the absorption of ozone. Aerosol attenuation coefficients depend on visibility at ground (vis), season, and eventual volcanic activity and are available for a few discrete sets only. The zenith angle of the Sun is calculated according to Iqbal.⁴⁸

In Table 1 we summarize the set of parameters taken as input for the model validation. Atmospheric parameters are set in a way that the results are as close as possible to the irradiance measurements at the sea surface. The separately named wavelengths in Table 1 are those given in Subsection 5.A. A 2-nm wavelength interval is used to ensure the correct incorporation of inelastic scattering.

The phytoplankton concentration C was measured on water samples taken approximately half an hour before the radiometer measurements were started (Table 2). An increase in C with increasing depth can be observed in the sample data, which is not confirmed in the irradiance data. If C increases, we should observe an increasing slope of the logarithmic

Table 2. Measured Phytoplankton Concentration and Gelbstoff Absorption (Lambda 18)

Depth (m)	5	35	50
C (mg m ⁻³)	0.043	0.079	0.145
Depth (m)	6	36	51
$a_y(440\text{ nm})$ (m ⁻¹)	0.019	0.021	0.041

Table 3. Parameterization of β_P with b_P^a

Location	b_P at 514 nm (m^{-1})	β_P
Turbid harbor	1.822	β_P^{th}
Coastal ocean	0.217	β_P^{coo}
Clear ocean	0.035	β_P^{clo}
Pure water	0	$\beta_P = 0$

^aRef. 56.

plot of irradiances versus depth (Figs. 8–10). C in Table 1 is almost exactly the mean of the measured values and assumed to be constant with depth.

The laboratory measurements of a_y (440 nm) yield values from 0.019 to 0.041 m^{-1} (see Table 2).⁴⁷ Our value [a_y (440 nm) = 0.014 m^{-1}] is close to the measured values for depths smaller than 35 m; $s = 0.017 \text{ nm}^{-1}$ has been confirmed by Breves *et al.*⁴⁷ and differs from the typical value $s = 0.014 \text{ nm}^{-1}$.

The scattering coefficient was not measured during the cruise. The value of $b_P = 0.036 \text{ m}^{-1}$ adopted in the simulation is almost identical to the value of the clear-ocean case of Petzold's measurements of volume-scattering function (Table 3). Other scattering coefficient measurements in clear oceans, summarized by Kirk,¹³ confirm that $b_P = 0.036 \text{ m}^{-1}$; c_j is within the range given by Morel.⁴⁹

D. Results

In Figs. 8–11 the results of the validation at wavelengths of 429, 489, 555, and 641 nm are presented.

Figures 8–10 show logarithmic plots of the downward irradiance E_d simulated by the model (dashed lines) and measured with the radiometer (solid curves) versus depth (0–45 m). The thin dashed lines are identical to the results of the simulation but graphically shifted by two constant factors f to allow an easier comparison between measurement and simulation. The introduction of f is required owing to a limited set of aerosol attenuation coefficients (Subsection 5.C). Therefore it was not possible to simulate irradiances at the ocean surface level that

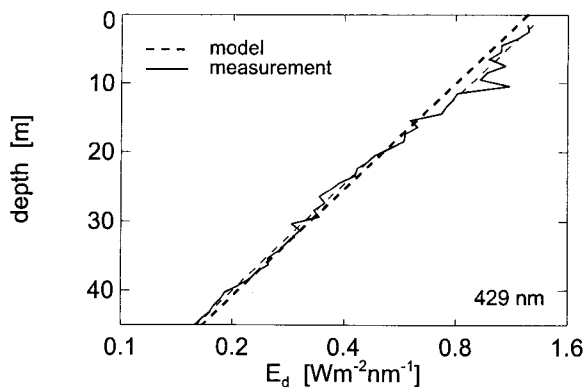


Fig. 8. Comparison of the measured and the simulated downward irradiance E_d at 429 nm.

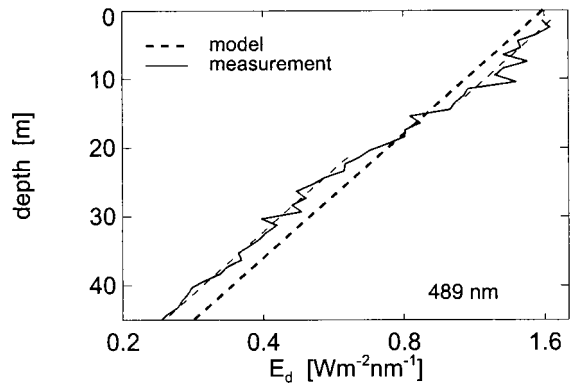


Fig. 9. Comparison of the measured and the simulated downward irradiance E_d at 489 nm.

are identical with those measured with the radiometer. The factor f was determined by minimizing

$$\sum_{i=1}^N [(E_d^M(z_i) - fE_d^S(z_i)/E_d^M(z_i))]$$

with E_d^M and E_d^S being the measured and the simulated downward irradiances, respectively, and N being the number of depth-dependent values between 0 and 45 m; f differs only slightly from one.

The second f is required owing to the increased

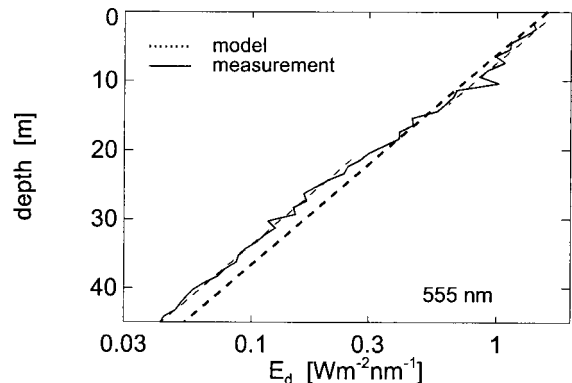


Fig. 10. Comparison of the measured and the simulated downward irradiance E_d at 555 nm.

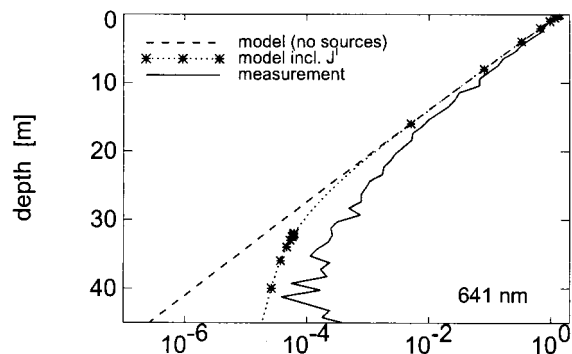


Fig. 11. Comparison of the measured and the simulated downward irradiance E_d at 641 nm.

slope in the measured irradiance at a depth of around 20 m. The fluorescence signals in Fig. 7 do not portend an increase in attenuation by an increase in gelbstoff or phytoplankton concentrations at a depth of around 20 m. The assumption of an increased accumulation of particles at a 20-m depth is not supported by temperature and salinity measurements (see Fig. 6). The given profiles would support a particle accumulation due to an increased density gradient at a depth of ~55 m but not at around 20 m. The increasing attenuation with depth might be caused by a cloudy sky. The jagged appearance of the measured irradiances can be explained by sea surface effects.

Figure 11 presents a comparison of the measured downward irradiance (solid curve) with the model results, the dotted line showing E_d including the inelastic sources J^I and the dashed curve showing E_d without these sources. The simulated E_d in the presence of inelastic sources has a similar course as the measured E_d but smaller absolute values. Comparing the slopes of the simulated and measured E_d for depths smaller than 20 m shows a slower decrease in the measured E_d , indicating an attenuation coefficient that is too small as a reason for the discrepancy. Increasing, e.g., water absorption at 641 nm by 6% would suspend the discrepancy. The absorption of pure water is still subject to controversy.^{50,51} A second reason for the discrepancy could be an error made during the generation of the calibration coefficients for the radiometer. Furthermore, incorrect dark-current subtractions are possible even though the dark currents are measured for each irradiance measurement. Because of generally small intensities at 641 nm, small errors in the calibration procedure would result in relatively large errors during field measurements.

The error between simulation and measurement is determined by $100(E_d^M - fE_d^S)/E_d^M$. The factor f is included to derive error estimations independent of the atmospheric model. If we do not consider a depth range of 14–21 m and E_d at 641 nm, we get a maximum difference of 22.8%. Closer investigation reveals that all differences greater than ~5% coincide with relatively extreme peaks in the measured data (Figs. 8–10), which might be explained by disturbing effects such as waves. At all three wavelengths the difference fluctuates around zero and shows no tendency to higher or lower values, suggesting a well presented depth dependency by the model. With a maximum difference of 5% in view of the accuracy of the radiometer (5.8%), the agreement between the model and the measurements is excellent for these three wavelengths.

The validation of the model needs to be extended with emphasis on inelastic sources. Measurements of E_d and other parameters in layered water columns, different oceans, and coastal regions must be approached. Extension of the matrix operators to the atmospheric part of the model would be appropriate. A comparison with other models⁵² is planned in the near future.

6. Simulated Effect of Inelastic Scattering

In the simulation of the effect of gelbstoff and chlorophyll fluorescence as well as water Raman scattering on underwater daylight, attention is focused on the depth dependency of the upward and downward irradiances and on the upward radiance being the most relevant value for the remote sensing of ocean color.

The parameters driving the simulations are mainly in Table 1. The Sun zenith angle is set to 20° and visibility to 50 km (summer model). The slope parameter for gelbstoff absorption is set to 0.014 nm⁻¹. The phytoplankton concentration (0.03, 0.1, 0.5, 5, and 30 mg m⁻³) and the absorption coefficient of gelbstoff at 440 nm (0.01, 0.1, 1, and 5 m⁻¹) are chosen to cover a wide variability found in the open ocean and coastal waters.^{10,12,13} The wavelength ranges from 400 to 700 nm with increments of 2 nm and from 250 to 650 nm with increments of 5 nm for water Raman scattering and chlorophyll fluorescence and gelbstoff fluorescence, respectively. We consider a homogeneous water body. The particle-scattering coefficient is determined by⁵³ (in m⁻¹)

$$b_p(\lambda) = 0.3 \left(\frac{550 \text{ nm}}{\lambda} \right) C^{0.62}. \quad (36)$$

A consequence is an indirect parameterization of the phase function with the phytoplankton concentration. An investigation of the possible dependencies of the inelastic fraction on the phase function and scattering coefficient as well as atmospheric conditions is discussed elsewhere or left open, respectively. Phase function and scattering coefficient dependencies have been found to be weak for case 1 waters.⁵ The dependency on Sun zenith angles has not been investigated in detail, but an exemplary simulation confirms results found by Gordon⁵ and Waters⁶: An increasing Sun zenith angle leads to the increasing effect of inelastic scattering, which is less dominant as wavelength or water constituent dependencies.

A. Effect on Ocean Color

The relevance of water Raman scattering for the remote sensing of ocean color is discussed first. As a measure of the relevance we define the inelastic fraction $100(L_{R+C}^- - L^-)/L_{R+C}^-$ for the upward nadir radiance just below the ocean surface [here $L^- = L^-(0^-; 0^\circ)$]. The index $R + C$ indicates the incorporation of water Raman scattering and chlorophyll fluorescence. The wavelengths relevant to ocean color are, among others, 490, 510, 560, and 620 nm.¹²

Figure 12 shows the dependency of the inelastic fraction on gelbstoff absorption and wavelength. At a phytoplankton concentration of 0.03 mg m⁻³ the inelastic fraction was determined for the set of gelbstoff absorption coefficients given above.

For $a_y(440 \text{ nm}) = 0.01 \text{ m}^{-1}$ we find fractions starting at around 10% at wavelengths close to 500 nm followed by a strong increase at 510–520 nm reaching values as high as 17%. With decreasing $a_y(440 \text{ nm})$ and small absolute values ($\leq 0.1 \text{ m}^{-1}$) a strong de-

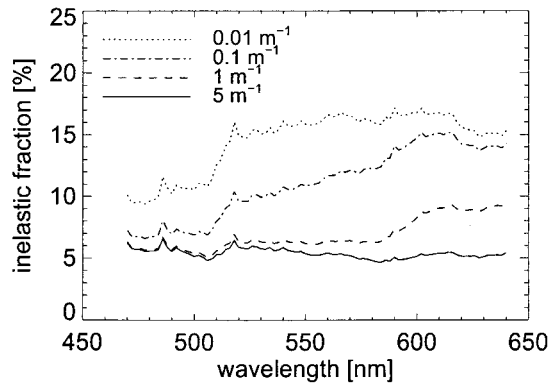


Fig. 12. Wavelength dependency of the inelastic fraction $J^{R,C}$ for the upward nadir radiance just below the ocean surface determined at four different gelbstoff absorptions at 440 nm ($C = 0.03 \text{ mg m}^{-3}$).

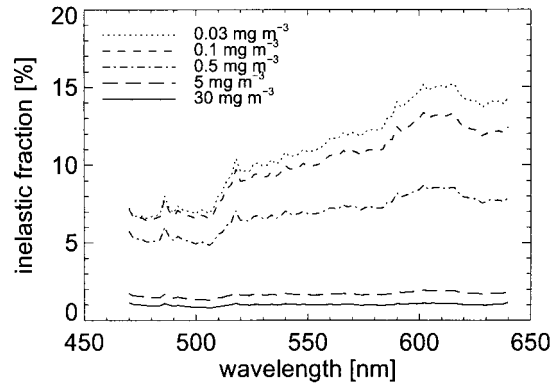


Fig. 13. Wavelength dependency of the inelastic fraction $J^{R,C}$ for the upward nadir radiance just below the ocean surface determined at five different phytoplankton concentrations [$a_y(440 \text{ nm}) = 0.1 \text{ m}^{-1}$].

crease in the fraction in the blue-wavelength range can be seen while the decrease in the red-wavelength range is small. This changes if $a_y(440 \text{ nm})$ becomes significantly large ($\geq 1 \text{ m}^{-1}$). In the red-wavelength domain the decrease in the fraction is now relatively large while the influence in the blue seems to level off. For largest $a_y(440 \text{ nm})$ and $C = 0.03 \text{ mg m}^{-3}$ we get an inelastic fraction of $\sim 5.5\%$, almost independent of the wavelength.

The results indicate that a further increase in gelbstoff absorption would result in a decrease in the inelastic fraction with wavelength. The first part of the observation can be explained by the strong decrease in gelbstoff absorption with increasing wavelength, thus having larger effects in the blue- than in the red-wavelength range. The independency of the inelastic fraction in the blue for a high $a_y(440 \text{ nm})$ might be interpreted as follows: With increasing gelbstoff absorption the amount of upward radiances from greater depths becomes smaller and smaller and at some point the dominant parameter governing the inelastic fraction is the coefficient of water Raman scattering, characterized by a strong decrease with increasing wavelength. A further effect arises from the spectral course of the excitation energy at the ocean surface, mainly influenced by the atmosphere. The downward irradiance at the ocean surface is generally characterized by a decrease in intensity for increasing wavelengths in the green- and red-wavelength range. The steeper the slope, the stronger the inelastic fraction becomes. We suppose the spectral course to be a minor effect with the exception of absorption lines. These conclusions are supported by the results of Hu and Voss⁴ and Gordon.⁵

Figure 13 shows the dependency of the inelastic fraction on wavelengths for different phytoplankton concentrations. The gelbstoff absorption at 440 nm is set to 0.1 m^{-1} . In general the fraction decreases with increasing C for all simulated wavelengths. For low concentrations ($\leq 0.1 \text{ mg m}^{-3}$) and wavelengths smaller than 510 nm the fraction is around

7%. For wavelengths greater than 510 nm the fraction shows a strong wavelength dependency with maximum values around 15%, similar to small gelbstoff absorptions and a small C . For large phytoplankton concentrations ($\geq 5 \text{ mg m}^{-3}$) the wavelength dependency vanishes and the fraction is less than 2%. The transition between both extremes occurs for $0.1 \leq C \leq 5 \text{ mg m}^{-3}$. In opposition to the lack of dependency of the fraction for large $a_y(440 \text{ nm})$ in the blue-wavelength domain the fraction decreases slightly for an increasing large C . Here the parameterization of the phase function with C results in increased backscattering,¹⁴ which lowers the fraction. Even though different bio-optical models have been implemented, our simulations of the inelastic fraction (clear water cases) lie between the results of Gordon⁵ and Waters⁶ (in the latter case if the upward irradiances are considered). The spectral course is almost identical to the findings of Waters,⁶ and changes in the phytoplankton concentration have a similar effect on the inelastic fraction for upward irradiance. The strong decrease in the fraction for $0.1 \leq C \leq 5 \text{ mg m}^{-3}$ was also found by Gordon⁵ but with generally higher fractions.

The previous findings have been received with gelbstoff fluorescence excluded. Since the effect of water Raman scattering generally decreases with decreasing water clarity, while gelbstoff fluorescence increases with an increasing gelbstoff load (at least if all other optically relevant water constituents are constant), gelbstoff fluorescence can have higher inelastic fractions than water Raman scattering at short wavelengths.

To address this issue simulations have been performed where only gelbstoff fluorescence has been incorporated. In Fig. 14 the wavelength dependency of the inelastic fraction is shown for three different combinations of gelbstoff absorption and phytoplankton concentration. All graphs have an underlying Gaussian shape that is modulated by relatively strong variations in the inelastic fraction between 250 and 430 nm. The extreme values coincide with

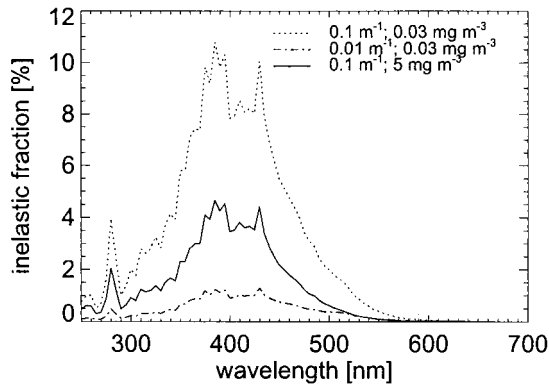


Fig. 14. Wavelength dependency of the inelastic fraction J^Y for the upward nadir radiance just below the ocean surface determined at three different combinations of the gelbstoff absorption (the first value in the legend) and the phytoplankton concentration (the second value in the legend).

minima in the solar spectrum,⁵⁴ in particular at 280 and 375 nm. The latter is the reason that the maximum of the inelastic fraction occurs around 375 nm and not at 425 nm. The maximum observed fraction of all three simulations is 11% at 375 nm [a_y (440 nm) = 0.1 m^{-1} and $C = 0.03 \text{ mg m}^{-3}$]. If the gelbstoff absorption decreases while the phytoplankton concentration is kept fixed, the inelastic fraction decreases. If a_y is kept fixed [here a_y (440 nm) = 0.1 m^{-1}] and C increases, the inelastic fraction decreases. The inelastic fractions at 470 nm, 1.5% at a_y (440 nm) = 0.1 m^{-1} and $C = 5 \text{ mg m}^{-3}$ and 4% at a_y (440 nm) = 0.1 m^{-1} and $C = 0.03 \text{ mg m}^{-3}$, are in the same order as the corresponding cases in Figs. 12 and 13, respectively. The conclusion is that gelbstoff fluorescence has a significant effect on ocean color, which can reach or even exceed the relevance of water Raman scattering. In fact an additional simulation [a_y (440 nm) = 1 m^{-1} and $C = 0.03 \text{ mg m}^{-3}$] revealed an inelastic fraction at 470 nm, ~ 4 times higher than the corresponding water Raman scattering fraction.

B. Depth Dependency

First, the importance of water Raman scattering and chlorophyll fluorescence for underwater daylight is demonstrated. We chose a_y (440 nm) = 0.1 m^{-1} and $C = 0.5 \text{ mg m}^{-3}$, both centered in the range of values found in nature.

Figures 15 and 16 show the depth dependency of the inelastic fraction for five selected wavelengths determined from the upward and the downward irradiances, respectively. The inelastic fraction for the upward irradiance shows a decrease in depth for small wavelengths (500 nm) until the contribution of inelastic scattering to underwater daylight is negligible. As the wavelength increases the decrease turns into an increase (580 nm) and finally reaches 100% (596 nm, 64 m). When the effect of inelastic scattering on the upward radiance (Subsection 6.A) is discussed, the dependency of the inelastic fraction on the spectral course of the excitation energy, on the

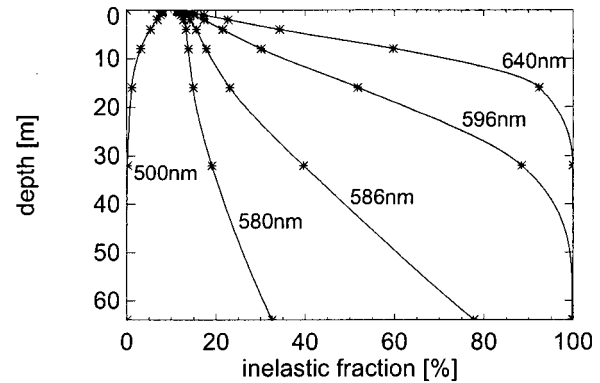


Fig. 15. Depth dependency of the inelastic fraction for the upward irradiance at five different wavelengths [$C = 0.5 \text{ mg m}^{-3}$, a_y (440 nm) = 0.1 m^{-1}].

water Raman scattering coefficient, and on the optical properties of the water body is pointed out. We concluded that the influence of b^R is relevant at the ocean surface. Considering the depth dependency of the fraction, the integrative effect of the total attenuation overcomes all other dependencies. As pointed out by Gordon⁵ the fraction should be proportional to $c(\lambda)/[c(\lambda) + c(\lambda')]$. At small wavelengths, e.g., 500 nm, the fraction decreases with depth because of the larger attenuation at smaller wavelengths, so the amount of excitation energy decreases faster than the energy at 500 nm. The opposite holds at larger wavelengths, e.g., 596 nm. The parameters defining the optical properties of the simulated water body result in a total attenuation coefficient that confirms the above statement. Between there is a transition range (580–600 nm) depending mainly on the total attenuation coefficient of the water body and, to a lower degree, on the alteration of the spectral course of the underwater daylight. If the absorption of phytoplankton and gelbstoff is large enough, the maximum of the light field is shifted from ~ 490 to ~ 550 nm. Hu and Voss⁴ found a transition between 500 and 550 nm but not the decrease at 500 nm. This is probably due to

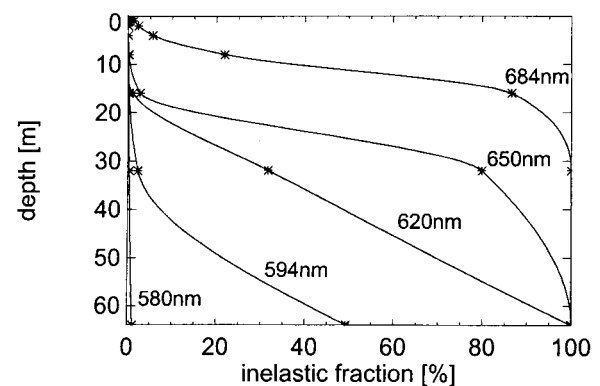


Fig. 16. Depth dependency of the inelastic fraction for the downward irradiance at five different wavelengths [$C = 0.5 \text{ mg m}^{-3}$, a_y (440 nm) = 0.1 m^{-1}].

different phytoplankton concentrations, apart from different bio-optical models. If the absorption of biogenic material is very low, then the increase in water absorption at around 510–520 nm might result in a transition between 500 and 550 nm. The total attenuation coefficient in our simulation does not show this increase owing to the dominance of gelbstoff and phytoplankton absorption over water absorption.

In Fig. 16 the inelastic fraction of the downward irradiance is plotted over depth for five different wavelengths. The larger the wavelength the faster the downward irradiances are dominated by inelastic scattering, reaching a level of 100% at wavelengths greater than 620 nm and depths smaller than 64 m. The downward irradiances show a strong increase in fraction for wavelengths between 580 and 620 nm. This is in accordance with Hu and Voss.⁴ At 684 nm the fraction is approximately 10–15% larger over the considered depth range than at 650 nm, and the 100% level is reached at significantly lower depths. The additional contribution of chlorophyll fluorescence with its emission maximum at 685 nm explains the increase.

Hu and Voss⁴ presented depth-dependent measurements of inelastic fractions for the upward irradiance at 589 nm. For a phytoplankton concentration of 0.1 mg m⁻³ they found fractions of ~16% slightly below the ocean surface and ~49% at a depth of approximately 19 m. We calculated a fraction of 17.1% at the ocean surface and of 48.2% at a depth of 19 m, both for a wavelength of 588 nm and for $C = 0.1 \text{ mg m}^{-3}$ and $\alpha_y(440 \text{ nm}) = 0.1 \text{ m}^{-1}$. These results are in good agreement with the measurements of Hu and Voss⁴ and can be a further validation of the model.

The depth dependency of the effect of gelbstoff fluorescence has been determined based on the simulations introduced in Subsection 6.A. For all simulations the maximum inelastic fraction of the downward irradiance is smaller than 0.15% for depths smaller than 50 m and wavelengths larger than 400 nm. The inelastic fraction of the upward irradiance is in all cases slightly larger than the corresponding values for the upward nadir radiance and exhibits an exponential decrease with depth for wavelengths around 425 nm. As expected from the discussion above this decrease is more rapid if the total attenuation increases.

7. Conclusions

A radiative-transfer model based on the matrix-operator theory is presented. The algorithm is not restricted concerning the optical properties of the water column and can be applied to case 1 and case 2 waters. All scattering orders are determined, and the wavelength dependency of the phase function is considered. Different options for the determination of $\tilde{\beta}$ are provided; among them is the indirect parameterization of Petzold's phase functions with the phytoplankton concentration. The algorithm is very efficient in computing underwater daylight for homogeneous water bodies, supported by the introduction

of vector operators $\tilde{\beta}_0^\pm$ (phase function vectors for the solar zenith angle).

To the knowledge of the authors, this is the first matrix-operator model capable of calculating gelbstoff and chlorophyll fluorescence as well as water Raman scattering. A detailed mathematical description and an exact methodology to account for the depth dependency of inelastic sources are given. The model allows the investigation of each of the inelastic sources separately and a comparison of their effects with computed light fields dominated by elastically scattered light alone.

A first successful approach of the validation of the algorithm was done with the help of depth and spectrally dependent radiometric measurements of the downward irradiance. The validation should be extended to other water bodies and parameters such as upward irradiances or water-leaving radiances. The validation of the inelastic scattering processes should be intensified. A comparison with other models is planned, and the need for an advanced atmospheric model is obvious.

The model offers the opportunity to avoid misinterpretations of parameters retrieved from *in situ* radiometric measurements. The combined application of radiometers and radiative-transport models, after matching the spectrally and depth-dependent results of the model and measurement, would allow an immense extension of the amount of retrievable parameters by inversion techniques, including information on water constituents such as phytoplankton concentration.

The investigation of the effect of inelastic scattering reveals its great relevance to the underwater light field. We separately simulated the dependency of the inelastic fraction $J^{R,C}$ on the phytoplankton concentration and the absorption of gelbstoff. Both dependencies were found to be significant. At wavelengths relevant to the remote sensing of ocean color the Raman fraction for the water-leaving radiance can reach values of more than 17% [$C = 0.03 \text{ mg m}^{-3}$ and $\alpha_y(440 \text{ nm}) = 0.01 \text{ m}^{-1}$]. For high phytoplankton concentrations the wavelength dependency vanishes and the inelastic fraction is smaller than 2%. In between there is a transition strongly dependent on C . For $C = 0.5 \text{ mg m}^{-3}$ the inelastic fraction is >6.5% at wavelengths greater than 520 nm.

The effect of increasing gelbstoff absorption obviously revealed the dependency of the inelastic fraction on the spectral course of the gelbstoff absorption. The decrease in fraction reached a minimum even though the absorption still increased demonstrating its dependency on the water Raman scattering coefficient. For $C = 0.03 \text{ mg m}^{-3}$ and wavelengths greater than 520 nm the fraction decreased from ~17% [$\alpha_y(440 \text{ nm}) = 0.01 \text{ m}^{-1}$] to ~5.5% [$\alpha_y(440 \text{ nm}) = 5 \text{ m}^{-1}$]. In general the fraction depends on the spectral course of the excitation energy, the Raman-scattering coefficient, and the optical properties of the water body, more precisely on $c(\lambda)/[c(\lambda) + c(\lambda')]$.

The presented inelastic fractions of gelbstoff fluorescence exhibit a maximum value of 11% [$C = 0.03$

mg m^{-3} , $a_y(440 \text{ nm}) = 0.1 \text{ m}^{-1}$]. The effect is of the same order as the effect of water Raman scattering and can exceed the water Raman scattering if a_y and C are relatively high [$a_y(440 \text{ nm}) = 1 \text{ m}^{-1}$] and low ($C = 0.03 \text{ mg m}^{-3}$), respectively. The main spectral features are given by the redistribution function and the spectral shape of the excitation energy.

Consideration of the depth dependency of the Raman fraction based on the upward and the downward irradiances [$C = 0.5 \text{ mg m}^{-3}$, $a_y(440 \text{ nm}) = 0.1 \text{ m}^{-1}$] shows a Raman effect mainly dependent on $c(\lambda)/[c(\lambda) + c(\lambda')]$. For wavelengths larger than 620 nm the fraction based on the downward irradiance reaches a level of 100% at 64 m. The fraction based on upward irradiances exceeds values of 100% at smaller wavelengths. Given a larger absorption at excitation wavelengths than at emitting wavelengths, a decrease in the Raman fraction at 500 nm has been observed. With the exception of near-surface layers and high gelbstoff absorptions, the effect of gelbstoff fluorescence on the depth dependency of irradiances is relatively low compared with the corresponding effect of water Raman scattering.

The results agree well with recently found inelastic fractions and serve as further validation.

Appendix A: Phase Function

The phase function $\tilde{\beta}$ gives the angular distribution of the scattered light and is defined as $\tilde{\beta}(\psi; \lambda) = \beta(\psi; \lambda)/b(\lambda)$, where ψ is the scattering angle, b is the total scattering coefficient, and β is the total volume scattering function. Each component in the medium that scatters light contributes to $\tilde{\beta}$:

$$\tilde{\beta}(\psi; \lambda) = \sum_i \frac{b_i(\lambda)}{b(\lambda)} \tilde{\beta}_i(\psi), \quad (\text{A1})$$

where i is an index referring to the scattering component. The phase function is explicitly wavelength dependent. In our algorithm this wavelength dependency is taken into account.

The algorithm enables the user to select between volume scattering functions calculated with Mie theory⁵⁵ and those measured by Petzold.⁵⁶ Using a Mie scattering code, we can estimate the scattering due to phytoplankton and transparent particles. Contributions from other scattering components to the phase function can easily be added.

The second option of our algorithm in computing the phase function is use of the Petzold volume scattering functions. Petzold performed measurements of β at scattering angles ranging from 0.1° to 180° in the harbor of San Diego, the coastal ocean, and the open ocean.⁵⁶ After subtraction of the pure seawater volume scattering function and the pure seawater scattering coefficient from β and b , respectively, we parameterize each particle volume scattering function β_p with the corresponding particle scattering coefficient b_p (Table 3): If b_p is known, the related volume scattering function can be interpolated. If b_p is greater than the scattering coefficient for the turbid harbor, then β_p^{th} (where *th* is the turbid har-

bor) is used. Otherwise the normalization of the phase function is difficult to realize (Appendix B).

Appendix B: Normalization

The phase function must satisfy the normalization condition

$$2\pi \int_{-1}^1 \tilde{\beta}(\mu; \lambda) d\mu = 1. \quad (\text{B1})$$

Owing to the combination of the discretization and the very strong emphasis on the forward direction of phase functions in natural water bodies, meeting Eq. (B1) is a challenging task. To make phase functions with strong forward peaks easier to handle, they can be prepared by so-called phase-function truncation techniques. This is based on the assumption that the distinction between forward-scattered and non-scattered light is in principle not possible. We assume that a certain amount of forward-scattered light can be considered nonscattered⁵⁷:

$$\tilde{\beta}(\mu' \rightarrow \mu; \lambda) = \alpha(\lambda)\delta(1, \mu) + [1 - \alpha(\lambda)]\tilde{\beta}'(\mu' \rightarrow \mu; \lambda), \quad (\text{B2})$$

where α is the part we consider nonscattered. An important consequence is that by modifying phase-function inherent optical properties like the beam attenuation coefficient c , the single-scattering albedo ω_0 and the optical depth τ will be altered.¹⁸ A user-defined minimum error ϵ is introduced to govern the accuracy of the algorithm [c_i from Eq. (12)]:

$$\left| \frac{1}{2\pi} - \sum_{i=1}^N [\tilde{\beta}(\mu_{1'} \rightarrow \mu_i; \lambda) + \tilde{\beta}(\mu_{1'} \rightarrow -\mu_i; \lambda)] c_i \right| < \epsilon. \quad (\text{B3})$$

In praxis the phase-function truncation is accomplished by cutting off the phase function for small scattering angles. The user of the model chooses the number of abscissas N and the accuracy ϵ , from which a cutoff angle θ_p follows, where the modified phase function $\tilde{\beta}'$ joins the original phase function $\tilde{\beta}$ to ensure normalization. In the determination of irradiances the phase-function truncation suggested above should lead to sufficient accuracies.¹⁸

The modified phase function $\tilde{\beta}'$ is continued between 0° and θ_p by the Henyey–Greenstein function:

$$\tilde{\beta}_{\text{HG}}(g; \psi) = \frac{1 - g^2}{4\pi[(1 + g^2 - 2g \cos \psi)]^{3/2}}, \quad (\text{B4})$$

where g is a parameter governing the slope of the Henyey–Greenstein function. The slope should be as steep as possible but should not let $\tilde{\beta}'$ become greater than $\tilde{\beta}$ at any angle.

The α value is calculated by the difference between the integrals of $\tilde{\beta}$ and $\tilde{\beta}'$, each integration done by the trapezoidal rule. If the Petzold phase functions are used, the integral for $\psi \in [0.1^\circ, 180^\circ]$ is determined

first. Depending on the result, $\tilde{\beta}$ is extended to 0° by the linear function of an appropriate gradient.

The conservation of energy is an important issue in radiative-transfer processes and is a direct consequence of the normalization of the phase function. To ensure energy conservation, the diagonal elements of $\tilde{\beta}^{++}$ (Subsection 2.B) will be corrected for the difference between the actual and the requested normalization value:

$$\tilde{\beta}''(\mu_{j'} \rightarrow \mu_j; \lambda) = \tilde{\beta}'(\mu_{j'} \rightarrow \mu_j; \lambda) + \frac{\Delta E(\mu_{j'}; \lambda)}{c_j}. \quad (\text{B5})$$

From approximation (B3) it follows for ΔE that

$$\Delta E(\mu_{j'}; \lambda) = \frac{1}{2\pi} - \sum_{i=1}^N [\tilde{\beta}'(\mu_{j'} \rightarrow \mu_i; \lambda) + \tilde{\beta}'(\mu_{j'} \rightarrow -\mu_i; \lambda)]c_i. \quad (\text{B6})$$

Appendix C: Atmosphere and Ocean Surface

Bartsch *et al.*⁵⁸ has developed a radiative-transfer model to investigate the influence of sunlight on the signal of a satellite-based lidar. Using measurements of the sunlight at the outermost part of the atmosphere,⁵⁴ their model determines the direct downward irradiance $E_d^{\text{dir}}(0^+)$ and the diffuse downward radiance $L^{\text{df}}(0^+)$ just above the ocean surface as an interim result. The interim results are used as input for the matrix operator model described here.

Coupling the atmosphere and the ocean contains physical and numerical difficulties. The physical problems arise from a wind-driven ocean surface. This complication is avoided when a flat surface that can be treated by using the Fresnel equations for reflection and refraction is assumed.⁵⁹ The numerical problems would require special treatment of the weights and abscissas of the quadrature due to non-linear mapping of the atmospheric on the oceanic abscissas.¹⁸ Two completely different models are coupled, one for the atmosphere and one for the ocean, and therefore we have two separate sets of abscissas and weights.

In the matrix-operator theory the ocean surface is treated as a layer of infinitesimal optical thickness. Reflection and transmission operators need to be introduced with special attention to the abscissas and to total reflection (μ_c , cosine of the critical angle):

$$\mathbf{r}_{OO} = \begin{cases} R_{OO}(\mu_i; n_O/n_A) & \mu_i^O \in [1, \mu_C] \\ 1 & \mu_i^O \in [\mu_C, 0] \end{cases}, \quad (\text{C1})$$

$$\mathbf{r}_{AA} = R_{AA}(\mu_i; n_A/n_O) \quad \mu_i^A \in [1, 0], \quad (\text{C2})$$

$$\mathbf{t}_{OA} = \begin{cases} T_{OA}(\mu_i; n_A/n_O) \left(\frac{n_A}{n_O}\right)^2 & \mu_i^O \in [1, \mu_C] \\ 0 & \mu_i^O \in [\mu_C, 0] \end{cases}, \quad (\text{C3})$$

$$\mathbf{t}_{AO} = \begin{cases} T_{AO}(\mu_i; n_O/n_A) \left(\frac{n_O}{n_A}\right)^2 & \mu_i^A \in [1, 0]. \end{cases} \quad (\text{C4})$$

The transmission T and the reflection R are taken from Hecht.⁵⁹ The term n stands either for the refractive index of the ocean (index O) or for the refractive index of the atmosphere (index A). Although \mathbf{r}_{OO} , the reflection of diffuse oceanic radiation, is incorporated by the adding procedure \mathbf{t}_{AO} , the transmission of atmospheric radiation into the ocean, is treated separately: First the transmission of light through the ocean surface into the ocean is determined and then interpolated with respect to the ocean abscissas. In a similar way the remaining transmission and reflection operators are treated while the source operator for the ocean surface layer is zero.

This work was supported by the Ministry of Research and Technology, Bonn, within the framework of the German JGOF'S Indian Ocean program. We are grateful to the captain and crew of the RV Sonne for support and to R. Heuermann and N. Bürckel for participation in the cruise and support in the data analysis. The chlorophyll data were made available by Nikolei Delling from the Institut für Biogeochemie und Meereschemie, Universität Hamburg, which is gratefully acknowledged. We thank M. Babin and D. Stramski for providing phytoplankton absorbance data. We are indebted to J. Fischer, F. Fell, and P. Albert for fruitful discussions on radiative-transfer theory. Finally, we thank the anonymous reviewers for suggestions that improved the paper.

References

1. Y. Ge, H. R. Gordon, K. J. Voss, and J. Kenneth, "Simulation of inelastic scattering contributions to the irradiance field in the ocean: variations in Fraunhofer line depths," *Appl. Opt.* **32**, 4028–4036 (1993).
2. V. I. Haltrin and G. W. Kattawar, "Self-consistent solution to the equation of transfer with elastic and inelastic scattering in ocean optics: 1. Model," *Appl. Opt.* **32**, 5357–5367 (1993).
3. B. R. Marshall and R. C. Smith, "Raman scattering and in-water ocean properties," *Appl. Opt.* **29**, 71–84 (1990).
4. C. Hu and K. J. Voss, "In situ measurements of Raman scattering in clear ocean water," *Appl. Opt.* **36**, 6962–6967 (1997).
5. R. H. Gordon, "Contribution of Raman scattering to water-leaving radiance: a reexamination," *Appl. Opt.* **38**, 3166–3174 (1999).
6. K. J. Waters, "Effects of Raman scattering on the water-leaving radiance," *J. Geophys. Res.* **100**, 13151–13161 (1995).
7. R. W. Gould and R. A. Arnone, "Remote sensing estimates of inherent optical properties in a coastal environment," *Remote Sens. Environ.* **61**, 290–301 (1997).
8. K. Günther, D. Ernst, and M. Maske, "Biophysical process of chlorophyll *a* fluorescence," in *The Use of Chlorophyll Fluorescence Measurements from Space for Separating Constituents of Seawater*, European Space Agency contract RFQ 3-5059/84/NL/MD, Vol. II [Gesellschaft zur Kernenergieverwertung in Schiffbau und Schifffahrt (GKSS), Forschungszentrum Geesthacht, Geesthacht, Germany, 1986].
9. K. G. Ruddick, H. J. Gons, M. Rijkeboer, and G. Tilstone, "Optical remote sensing of chlorophyll *a* in case 2 waters by use of an adaptive two-band algorithm with optimal error properties," *Appl. Opt.* **40**, 3575–3585 (2001).
10. J. Fischer and U. Kronfeld, "Sun-stimulated chlorophyll fluorescence. 1: Influence of oceanic properties," *Int. J. Remote Sens.* **11**, 2125–2147 (1990).

11. K. G. Ruddick, F. Ovidio, D. Van den Eynde, and A. Vasilkov, "The distribution and dynamics of suspended particulate matter in the Belgian coastal waters derived from AVHRR imagery," in *Proceedings of the Ninth Conference on Satellite Meteorology and Oceanography*, Paris, France, 25–29 May 1998 (American Meteorological Society, Boston, Mass., 1998) Vol. 2, pp. 626–629.
12. R. Doerffer and H. Schiller, "Pigment index, sediment and gelbstoff retrieval from directional water-leaving radiance reflectances using inverse modeling techniques," ATBD 2.12, Tech. Rep. PO-TN-MEL-GS-0005 (ESA—European Space Research and Technology Center, Noordwijk, Netherlands, 1997).
13. J. T. O. Kirk, *Light and Photosynthesis in Aquatic Ecosystems* (Cambridge University, Cambridge, England, 1994).
14. C. D. Mobley, *Light and Water* (Academic, San Diego, Calif., 1994).
15. Z. Jin and K. Stamnes, "Radiative transfer in nonuniformly refracting layered media: atmosphere–ocean system," *Appl. Opt.* **33**, 431–442 (1994).
16. R. H. Stavn and A. D. Weidemann, "Optical modeling of clear ocean light fields: Raman scattering effects," *Appl. Opt.* **27**, 4002–4011 (1988).
17. G. N. Plass, G. W. Kattawar, and F. E. Catchings, "Matrix operator theory of radiative transfer. 1: Rayleigh scattering," *Appl. Opt.* **12**, 314–329 (1973).
18. F. Fell and J. Fischer, "Numerical simulations of the light field in the atmosphere–ocean system using the matrix-operator theory," *J. Quant. Spectrosc. Radiat. Transfer* **69**, 351–388 (2001).
19. V. A. Ambarzumian, "Diffusion of light by a foggy medium," *C. R. Acad. Sci. USSR* **38**, 229–232 (1943).
20. G. G. Stokes, "On the intensity of the light reflected from or transmitted through a pile of plates," *Proc. R. Soc. London* **11**, 545–556 (1862).
21. S. Chandrasekhar, *Radiative Transfer* (Dover, New York, 1960).
22. R. Redheffer, "On the relation of transmission-line theory to scattering and transfer," *J. Math. Phys.* **41**, 1–41 (1962).
23. R. W. Preisendorfer, *Radiative Transfer on Discrete Spaces* (Pergamon, New York, 1965).
24. I. Grant and G. Hunt, "Discrete space theory of radiative transfer I + II: fundamentals and stability and non-negativity," *Proc. R. Soc. London Ser. A* **313**, 183–197, 199–216 (1969).
25. A. H. Stroud and D. Secrest, *Gaussian Quadrature Formulas* (Prentice-Hill, Englewood Cliffs, N.J., 1966).
26. H. R. Gordon, "Diffuse reflection of the ocean: the theory of its augmentation by chlorophyll *a* fluorescence at 685 nm," *Appl. Opt.* **18**, 1161–1166 (1979).
27. E. D. Traganza, "Fluorescence excitation and emission spectra of dissolved organic matter in sea water," *Bull. Mar. Sci.* **19**, 897–904 (1969).
28. S. K. Hawes, C. K. Carder, and G. R. Harvey, "Quantum fluorescence efficiencies of fulvic and humic acids: effects on ocean color and fluorometric detection," in *Ocean Optics XI*, G. D. Gilbert, ed., *Proc. SPIE* **1750**, 212–223 (1992).
29. D. A. Kiefer and R. A. Reynolds, "Advances in understanding phytoplankton fluorescence and photosynthesis," in *Primary Productivity and Biogeochemical Cycles in the Sea*, P. G. Falkowski and A. D. Woodhead, eds. (Plenum, New York, 1992), pp. 155–174.
30. D. A. Kiefer, W. S. Chamberlin, and C. R. Booth, "Natural fluorescence of chlorophyll *a*: relationship to photosynthesis and chlorophyll concentration in the western South Pacific gyre," *Limnol. Oceanogr.* **34**, 868–881 (1989).
31. J. Fischer, R. Doerffer, and H. Grassl, "Factor analysis of multispectral radiances over coastal and open ocean water based on radiative-transfer calculations," *Appl. Opt.* **25**, 448–456 (1986).
32. R. Doerffer and J. Fischer, "Measurements and model simulations of Sun-stimulated chlorophyll fluorescence within a daily cycle," *Adv. Space Res.* **7**, 117–120 (1987).
33. S. A. Green and N. V. Blough, "Optical absorption and fluorescence properties of chromophoric dissolved organic matter in natural waters," *Limnol. Oceanogr.* **39**, 1903–1916 (1994).
34. P. G. Coble, "Characterization of marine and terrestrial DOM in seawater using excitation-emission matrix spectroscopy," *Mar. Chem.* **51**, 325–346 (1996).
35. G. E. Walrafen, "Raman spectral studies of the effects of temperature on water structure," *J. Chem. Phys.* **47**, 114–126 (1967).
36. A. H. Chang and L. A. Young, "Seawater temperature measurement from Raman spectra," AVCO Everett Research Laboratory Res. Note 960, (AVCO Everett Research Laboratory, Everett, Mass., 1974), pp. 82.
37. J. S. Bartlett, K. J. Voss, S. Sathyendranath, and A. Vodacek, "Raman scattering by pure water and seawater," *Appl. Opt.* **37**, 3324–3332 (1998).
38. G. E. Walrafen, "Continuum model of water—an erroneous interpretation," *J. Chem. Phys.* **50**, 567–569 (1969).
39. S. P. S. Porto, "Angular dependency and depolarization ratio of the Raman effect," *J. Opt. Soc. Am.* **56**, 1585–1589 (1966).
40. W. Breves and R. Reuter, "Bio-optical observations of gelbstoff in the Arabian Sea at the onset of the southwest monsoon," *Proc. Indian Acad. Sci. (Earth Planet. Sci.)* **109**, 415–425 (2000).
41. R. Heuermann, R. Reuter, and R. Willkomm, "RAMSES: a modular multispectral radiometer for light measurements in the UV and VIS," in *Environmental Sensing and Applications*, M. Carler, M. Hilton, T. Lamp, R. Reuter, K. Schaefer, G. M. Russwurm, K. Weber, K. Weitkamp, J. Wolf, and L. Woppowa, eds., *Proc. SPIE* **3821**, 279–285 (1999).
42. R. M. Pope and E. S. Fry, "Absorption spectrum (380–700 nm) of pure water. II. Integrating cavity measurements," *Appl. Opt.* **36**, 8710–8723 (1997).
43. R. C. Smith and K. S. Baker, "Optical properties of the clearest natural waters (200–800 nm)," *Appl. Opt.* **20**, 177–184 (1981).
44. L. Prieur and S. Sathyendranath, "An optical classification of coastal and oceanic waters based on the specific spectral absorption curves of phytoplankton pigments, dissolved organic matter, and other particulate materials," *Limnol. Oceanogr.* **26**, 671–689 (1981).
45. M. Babin and D. Stramski, "Light absorption by aquatic particles in the near-infrared spectral region," *Limnol. Oceanogr.* **47**, 911–915 (2002).
46. A. Bricaud, A. Morel, and L. Prieur, "Absorption by dissolved organic matter of the sea (yellow substance) in the UV and visible domains," *Limnol. Oceanogr.* **26**, 43–53 (1981).
47. W. Breves, R. Heuermann, and R. Reuter, "Enhanced red fluorescence emission in the oxygen minimum zone of the Arabian Sea," *Ocean Dyn.* (to be published).
48. M. Iqbal, *An Introduction to Solar Radiation* (Academic, New York, 1983).
49. A. Morel, "Diffusion de la lumiere par le aux de mer. Resultats Experimentaux et approche theorique," in *Light in the Sea*, J. E. Tyler, ed. (Dowden, Hutchinson and Ross, Stroudsburg, Pa., 1977), pp. 65–97.
50. T. I. Quickenden, C. G. Freeman, and R. A. J. Litjens, "Some comments on the paper by Edward S. Fry on the visible and near-ultraviolet absorption spectrum of liquid water," *Appl. Opt.* **39**, 2740–2742 (2000).
51. E. S. Fry, "Reply to criticisms of the Pope and Fry paper on pure water absorption made in a comment by T. I. Quickenden, C. G. Freeman, and R. A. J. Litjens," *Appl. Opt.* **39**, 5843–5846 (2000).
52. A. D. Mobley, B. Gentili, H. R. Gordon, Z. Jin, G. W. Kattawar, A. Morel, P. Reinersman, K. Stamnes, and R. H. Stavn, "Com-

- parison of numerical models for computing underwater light fields," *Appl. Opt.* **32**, 7484–7504 (1993).
53. H. R. Gordon and A. Morel, "Remote assessment of ocean color for interpretation with satellite visible imagery, a review," in *Lecture Notes on Coastal and Estuarine Studies*, Vol. 4, M. Bowman, ed. (Springer-Verlag, New York, 1983), pp. 1–114.
 54. G. Thuillier, M. Herse, P. C. Simon, D. Labs, H. Mandel, D. Gillotay, and T. Foujols, "The visible solar spectral irradiance from 350 to 850 nm as measured by the SOLSPEC spectrometer during the ATLAS-1 mission," *Sol. Phys.* **177**, 41–61 (1998).
 55. G. Mie, "Beiträge zur Optik trüber Medien, speziell kolloidaler Metall-Lösungen," *Ann. Phys.* **25**, 377–445 (1908).
 56. T. J. Petzold, "Volume scattering functions for selected ocean waters," SIO Ref. 72–78 (Scripps Institution of Oceanography, San Diego, Calif., 1972).
 57. J. F. Potter, "The delta function approximation in radiative transfer theory," *J. Atmos. Sci.* **27**, 943–949 (1970).
 58. B. Bartsch, T. Braeske, and R. Reuter, "Oceanic lidar: radiative transfer in the atmosphere at operating altitudes from 100 m to 100 km," *Appl. Opt.* **32**, 6732–6741 (1993).
 59. A. Hecht, *Optik* (Addison-Wesley, Bonn, Germany, 1989).